Article

Ag-NP-Decorated Carbon Nanostructures: Synthesis, Characterization, and Antimicrobial Properties

Adriana Angelina Siller-Ceniceros, Dulce Carolina Almonte-Flores, M. Esther Sánchez-Castro, Eduardo Martínez-Guerra, Javier Rodríguez-Varela, Nora Aleyda García Gómez, and José Rubén Morones-Ramírez*

Read Online

ACCESS | Metrics & More | Article Recommendations

Carbon Matrix (Graphene oxide or Carbon nanoplatelets) → Carbon Matrix decorated with AgNPs → Interaction of Carbon Matrix decorated with AgNPs and *E. coli* → Antimicrobial Effect of the Carbon Matrix decorated with AgNPs
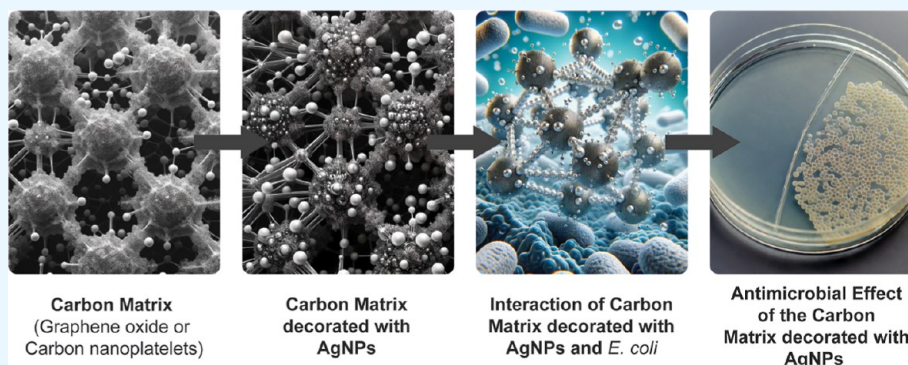
ABSTRACT: As the global urgency for effective antimicrobial agents intensifies, this work harnesses the widely demonstrated antimicrobial activity of silver nanoparticles (Ag-NPs) and proposes alternative synthesis approaches to metal−organic hybrid systems with antimicrobial activity. In this study, the proposed synthesis route involves decorating metallic nanoparticles into organic substrates without previous doping. The synthesis simultaneously uses polyethylene glycol for three crucial purposes: (1) acting as a mild reducing agent to generate Ag-NPs with a spherical shape and diameters ranging from 10 to just over 20 nm, (2) functioning as a dispersing agent for flakes of commercial nanostructured carbon supports, including reduced graphene oxide (rGO, ID-nano), and commercial carbon nanoplatelets from Sigma-Aldrich (GNPs, Sigma-Aldrich), and (3) serving as a promoter for the homogeneous anchoring of Ag-NPs in the carbon lattice without altering the conformation of the carbon lattice. This intricate interaction involves the π-orbitals from the sp^2 hybridization honeycomb and the d-orbitals from the Ag-NPs, leading to the constructive rehybridization of rGO and GNPs. In our study, Ag-NPs/rGO are compared with a support lacking oxygenated groups in the lattice, such as commercial GNPs (Sigma-Aldrich), to produce Ag-NPs/GNPs. This comparison maintains constructive sp^2 rehybridization, preserving the characteristic properties of rGO (ID-nano) and graphene nanoplatelets, including commercial GNPs (Sigma-Aldrich). Notably, oxygenated groups from rGO exhibit greater availability for exchanging oxo and hydroxy defects for Ag-NPs compared with GNPs (Sigma-Aldrich). The resulting Ag-NPs/rGO and Ag-NPs/GNP systems are thoroughly physicochemically characterized, employing techniques such as Fourier transform infrared spectroscopy, Raman spectroscopy, X-ray diffraction, scanning electron microscopy and energy dispersive X-ray spectroscopy, high-resolution transmission electron microscopy, and scanning transmission electron microscopy, revealing the successful integration of Ag-NPs with minimal alteration to the carbon lattice. Subsequent antimicrobial evaluation against *Escherichia coli* (*E. coli*) demonstrates significant activity, with Ag-NPs/rGO and Ag-NPs/GNPs registering similar minimum inhibitory concentrations of 50 μg mL^{-1}. This study underscores the potential of our metal−organic hybrid systems as antimicrobial agents and provides insights into the constructive rehybridization process, paving the way for diverse applications in the biomedical and environmental fields.

1. INTRODUCTION

At present, the use of silver nanoparticles (Ag-NPs) in hybrid materials has garnered considerable attention for their potential as antimicrobial agents.[1−4] Ag-NPs play a significant role in the cytotoxicity of microbial cell walls. However, the precise molecular mechanism of cellular toxicity induced by

Ag-NPs remains elusive.[5] However, it is suggested that Ag-NPs exhibit at least three main interactions that render them toxic to bacteria. The first interaction is that Ag-NPs possess an adhesive capacity to microbial cell walls, producing disruption of the intercellular molecule and inhibition of the electron transport chain (ETC) that causes the following cell damage: inhibition of cytoplasmic proteins, inhibition of membrane proteins, and inactivation of enzymes and metabolism.[6,7] Second, it is proposed that Ag-NPs, once they penetrate the bacteria, invade the bacterial respiratory chain due to their ionization to Ag^+ and interaction with oxygen, producing damage to nucleic acids and oxidative stress by reactive oxygen species (ROS).[8] The third factor can be attributed to silver ions causing interference with bacterial DNA, promoting the inhibition of DNA replication and transcription.[9]

Nevertheless, despite the toxic characteristics of Ag-NPs in bacteria, it is important to highlight that Gram-negative bacteria such as Escherichia coli (E. coli) carry a negative charge due to the external layer of peptidoglycan coating their layer of lipopolysaccharide in the cell wall, which prefers to stick to a positively charged surface, reducing their adhesion and bactericidal effect of Ag-NPs.[10] In the innovative study proposed by Das et al., a meticulous investigation of the reduced graphene oxide (rGO) protein nanoframework was characterized widely through various physicochemical characterization techniques and carefully assessed through assays demonstrating the antimicrobial mechanism of action of the antimicrobial rGO and their hybrid materials.[11−13] These analyses proposed the mechanism of disruption of the bacterial membrane in E. coli, inducing alterations in its potential and reducing the bacterial size. Consequently, this affects the surface membrane permeability, ultimately leading to cellular lysis and improving the killing efficiency. In addition, Das et al. described the rGO interaction with lipopolysaccharide and cell membrane proteins through hydrogen-bonding, $\pi-\pi$ stacking, and electrostatic interactions by making contact with the microorganism, resulting in physical disruption of the cellular membrane, which alters the transmembrane potential of the cells[13]

Moreover, studies conducted by Fathalipour et al. have demonstrated the synergistic effects of incorporating Ag-NPs onto carbonaceous materials with bioaffinity for biological systems, resulting in enhanced antimicrobial activity against Gram-negative and Gram-positive pathogenic microorganisms compared to the individual behavior of carbonaceous materials or Ag-NPs alone.[14] Similarly, another research work by Das et al. revealed the behavior of the hybrid material rGOAg, where it traverses the cytoplasm through the damaged membrane, inducing oxidative stress with intracellular reactive oxygen species (ROS, as hydrogen peroxide: H_2O_2, superoxide anions: $O_2^{\bullet-}$, hydroxyl radicals: $OH^{\bullet}$, or singlet molecular oxygen: $^1O_2$) production and subsequent metabolic events. Excessive ROS production produced lipid peroxidation, which disrupted cellular integrity. Additionally, ROS reduced the activity of the respiratory chain dehydrogenase, leading to metabolic arrest in the cells and ultimately resulting in the death of the microorganism.[11,12]

Furthermore, nanostructured carbon lattices based on graphene, such as rGO and GNPs, share a common feature of being conformed to graphitic lattices with sharp edges. This characteristic aids in causing significant mechanical damage to the bacterial cell membrane, leading to the leakage of intracellular material.[15] Nevertheless, the incorporation of Ag-NPs to decorate carbon lattices enhances their capacity to damage bacterial cell walls.

In a recent work, Malik et al. demonstrated the weight ratios of GNPs in the $(Ag)_{1-x}(GNPs)_x$ nanocomposites, ranging from 25 to 75% wt, with the highest bactericidal effect observed to Gram-negative and Gram-positive bacteria at 50% wt GNP loading. However, no high-resolution transmission electron microscopy (HR-TEM) images were provided to show the homogeneous distribution of Ag-NPs within the GNP lattice, not demonstrating their homogeneity.[16]

On the other hand, in a study conducted by Prasad et al. on rGO-nAg nanocomposites, HR-TEM micrographs revealed a high level of uniformity in the distribution of Ag-NPs within the rGO lattice. However, concentrations of 100 μg/mL were required to inhibit the growth of three different types of microorganisms.[17]

Carbon lattices GNPs and rGO have shown great potential as coadjuvants to enhance the antimicrobial properties of Ag-NPs. However, the traditional synthesis methods for incorporating metallic nanoparticles into different carbon lattices often involve the use of strong reducing agents such as sodium borohydride ($NaBH_4$) or hydrazine (N_2H_4), which are highly toxic and pose challenges for proper disposal.[18−20] Hence, there is a need to explore alternative chemical synthesis routes that facilitate the interaction between materials with biological affinity and physicochemical features to anchor Ag-NPs with homogeneous spherical morphology and particle size distribution, thereby exhibiting antimicrobial activity.[21,22]

The polyol method, coupled with the use of nanostructured graphitic carbon material, provides a promising approach for synthesizing Ag-NPs and decorating the carbon lattice to obtain Ag/C-type materials.[23] In this regard, the ethylene glycol (EG) of Ag-NPs acted as a dispersing medium for their uniform anchoring onto the nanostructured carbon lattice.

This approach was substantiated on the work by Rago et al., which highlighted the antimicrobial activity of pristine GNPs and their ability to cause mechanical damage by trapping and wrapping the cellular wall of bacteria, thereby enhancing the killing effect.[24]

Similarly, Geetha Bai et al. demonstrated cell membrane disruption attributed to the interaction between different pathogenic bacteria and rGO-Ag nanocomposite. The antimicrobial assay revealed minimum inhibitory concentrations (MICs) ranging from 65 to 125 μg/mL.[25]

Therefore, having in mind the enhancement of antimicrobial activity, in this study, hybrid systems Ag/rGO and Ag/GNPs were compared with pristine commercial nanostructured carbon lattices rGO (ID-nano) and GNPs (Sigma-Aldrich), respectively. Subsequently, they were subjected to Fourier transform infrared spectroscopy (FTIR), Raman spectroscopy, X-ray diffraction (XRD), scanning electron microscopy and energy dispersive X-ray spectroscopy (SEM−EDS), HR-TEM, and scanning transmission electron microscopy (STEM). Moreover, their antimicrobial properties were evaluated against E. coli (E. coli, ATCC-11229). In the hybrid systems synthesized: Ag/rGO and Ag/GNPs, the carbonaceous lattice was not significantly altered. This preservation ensures the retention of the inherent structural characteristics of the carbon lattice, even with the inclusion of metal nanoparticles. Maintaining the integrity of the powder carbon nanostructured lattice with Ag-NPs is advantageous for applications in biology such as antimicrobial agents and biosensors with biomedical applications.
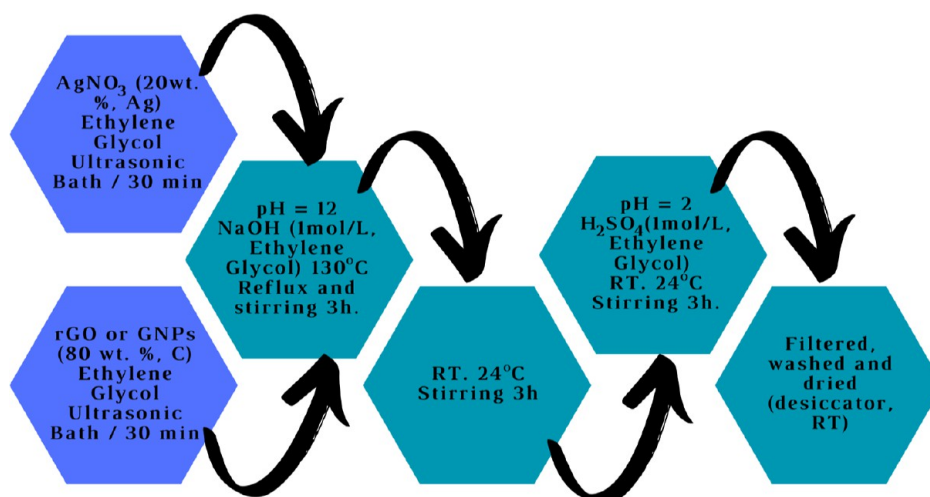
Figure 1. Scheme of the synthesis of Ag/rGO and Ag/GNP powders by the polyol process.

2. METHODOLOGY

2.1. Materials. Graphene nanoplatelets (grade C-750), silver nitrate ($AgNO_3$, ACS reagent, ≥99.0%), sulfuric acid (H_2SO_4), sodium hydroxide (NaOH), and ethylene glycol were sourced from Sigma-Aldrich. The Millipore filtration assembly and the Millipore filtration vacuum pump (37 L min^{-1}) were products of MERCK. pH calibration standards (4.00 ± 0.01, 7.00 ± 0.01, and 10.00 ± 0.01) were obtained from Thermo Fisher Scientific. The pH indicator paper (0–14) was a product of Whatman, while the pH meter was ST5000-F from Ohaus. Other supplies included membrane filters (polyamide pore size 0.45 μm and diameter 47 mm) from Whatman, a glass watch, a glass desiccator, silica gel, Luria–Bertani (LB) broth (Difco Miller), and 96-well plates (Costar) from Corning. The equipment used was as follows: Optizen 2120 UV: single beam UV–vis spectrophotometer; Multiskan spectrophotometer (Thermo Scientific); heated floor model shaking incubator (250 L, 230VAC, 50/60 Hz) from Lab Companion (model AAH23306K); ultrasonic cleaner bath VWR Symphony; high-performance lab refrigerator from Thermo Scientific TSX Series; and Vortex Mixer 3220 rpm/3350 rpm (GENIE2), drying oven (Shel Lab SGO5), A2 Biological Safety Cabinet with UV Light (LABCONCO), and ion exchange UV Ultrapure Water Purification System (Milli Q-Merck).

2.2. Synthesis of Ag/rGO and Ag/GNPs. The antibacterial compounds Ag/rGO and Ag/GNPs were synthesized utilizing the traditional polyol method.[26] This method involved the use of EG as a reducing agent. For the synthesis, an 80 mg allocation (representing 80 wt %) of specific nanostructured carbon substrates, labeled rGO and GNPs, was used.

Initially, 31.5 mg of $AgNO_3$ (20% Ag) was dispersed in 2 mL of EG for 30 min in a flask under ultrasonic conditions. The same procedure was performed separately using 80% wt of rGO or GNPs dispersed in 48 mL of EG.

The second step involved the dropwise addition of $AgNO_3$ to the rGO solution. This mixture was stirred for 30 min, and afterward, the pH was adjusted to 12 using 2.5 mL of NaOH (1 mol L^{-1} solution in EG). The resulting mixture was placed in a reflux system with magnetic stirring at 600 rpm. The reflux system was maintained at a temperature of 130 °C for a duration of 3 h.

In the third step, the solution was allowed to cool to room temperature and stirred for 3 h. Finally, the pH was adjusted to 2 by adding 4 mL of H_2SO_4 (1 mol L^{-1} solution in EG) and stirring at 600 rpm for 3 h. After completion of all the steps, the solution was filtered using a mixed cellulose ester filter. The obtained powder was then washed and dried at room temperature in a desiccator. The methodology is summarized in Figure 1.

2.3. Physicochemical Characterization. FTIR spectra were obtained in a PerkinElmer Spectrum 400 with a resolution of 4 cm^{-1}, and 32 scans were recorded using the attenuated total reflectance (ATR) technique in a range of 4000–350 cm^{-1} wavenumber. Raman microanalysis was performed in a Thermo Scientific DXR Raman microscope class I, with a 780 nm laser, an aperture of 50 mm, and a laser power of 5 mW in a range of 3000–100 cm^{-1}.

XRD patterns were acquired by an Empyrean PANalytical diffractometer with a Bragg–Brentano geometry, with the X-ray tube in line focus (Cu K$_\alpha$, 1.5418 Å) in a range of $2\theta = 10$–90° with a step size of 0.2° and 59 s per step.

To ascertain the crystallite dimensions for Ag/GNPs and Ag/rGO, the Debye–Scherrer equation[27] was employed

$$D = \frac{0.9\lambda}{\beta \times \cos\theta}$$

where D is the crystallite size, λ is the wavelength of K$_\alpha$ source of X-ray radiation, β is the full width at half-maximum of specific crystal reflection, and $\cos\theta$ is the 2θ value in radians of each crystal reflection place.

The chemical composition or chemical mapping was carried out in a Philips XL30 SEM, coupled with energy-dispersive X-ray spectroscopy (EDS). Specifically, the morphology reported in the case of *E. coli* was necessary to cover the cell wall with Trump's solution, as reported to biological material by Sarabia-Castillo et al., to fix the bacteria on the holder and take the images under a lower accelerating voltage of 5 kV.[28] On the other hand, all images of Ag/rGO, Ag/GNPs, and *E. coli* covered with these microbicide agents were obtained by SEM under an accelerating voltage of 10 kV.

HR-TEM was used to acquire the morphology and shape of Ag-NPs attached to Ag/rGO and Ag/GNPs. These materials were characterized by the Talos F200X G2, a 200 kV FEG scanning transmission electron microscope (S/TEM) under an

accelerating voltage of 200 kV, with a 0.16 nm resolution. The chemical mapping was obtained by an energy-dispersive X-ray from the same microscope.

2.4. Minimum Inhibitory Concentration. The evaluation of MICs was performed using the microdilution method, following established literature protocols.[29]

In the first step, an overnight culture (ON) of *E. coli* ATCC-11229 incubated at 37 °C and 150 rpm was inoculated. The culture was diluted 1:250 in fresh LB medium and incubated until a critical optical density (OD$_{600nm}$ of 0.2 ± 0.02). The OD$_{600nm}$ of the control was measured using a UV−vis spectrophotometer.

In the second step, the nanomaterials test procedure was conducted in a 96-well plate. A final concentration of 2000 mg/L was prepared for each nanomaterial, including rGO, GNPs, Ag/rGO, and Ag/GNPs, which were individually diluted in a LB broth. A total of 200 μL of the final solution were added to each well, and then 100 μL was transferred to the next well containing 100 μL of pristine LB broth, with the 100 μL from the last dilution. This dilution procedure was repeated until reaching a concentration of 62.5 mg/L of nanomaterial in 100 μL. The well-containing bacteria solution was added to each well, except for the sterility control (200 μL of pristine LB broth) and the growth control (200 μL of bacteria, OD$_{600nm}$ ± 0.02), which were placed in the first and second wells, respectively. Each carbon nanomaterial (rGO, GNPs, Ag/rGO, and Ag/GNPs) was evaluated in three separate assays, covering a concentration range from 1000 to 62.5 mg/L after the addition of bacteria.

In the last step, the 96-well plate was incubated at 37 °C and 150 rpm for 20 h. The ODs of the control and each nanomaterial treatment were measured every hour for a total of 24 h using a Multiskan GO microplate spectrophotometer.[30]

3. RESULTS AND DISCUSSION

3.1. Physicochemical Characterization. Figure 2 delineates the FTIR spectra comparisons between Ag/GNPs and GNPs and Ag/rGO and rGO. The GNPs FTIR spectrum exhibits very weak vibrational bands attributed to the C=C bond of the aromatic ring at 1439 and 1565 cm^{-1} (Figure 2a).[31] Similarly, weak signals present at 2164 and 2012 cm^{-1} are attributed to the symmetrical and asymmetrical C−H bonds at the terminal edges of the GNPs' carbon lattices.[31−33] Moreover, the vibrational band corresponding to the O−H bond of defects within the GNPs' carbon network is scarcely discernible, making its appearance around 3712 cm^{-1}.[34] Typically, FTIR signals stemming from graphitic-structured carbon are inherently weak. This phenomenon stems from the crystalline nature of the hexagonal, honeycomb network and the Janus behavior of the 2D carbon structures in predominantly graphitic materials, as reported in prior literature.[35]

In this study, the lattice structure of GNPs appears to overlap with the FTIR signals, leading to the cancellation of the vibrational responses arising from the stacking of graphitic layers inherent to pristine GNPs. Notably, the Ag/GNPs spectrum showcases a heightened intensity across all signals. This amplified response is credited to the interplay between the d-orbitals of silver atoms and the π-orbitals derived from the sp^2 hybridization of GNPs. This interaction induces an electronic change in the vibrational dynamics of the graphitic lattice.
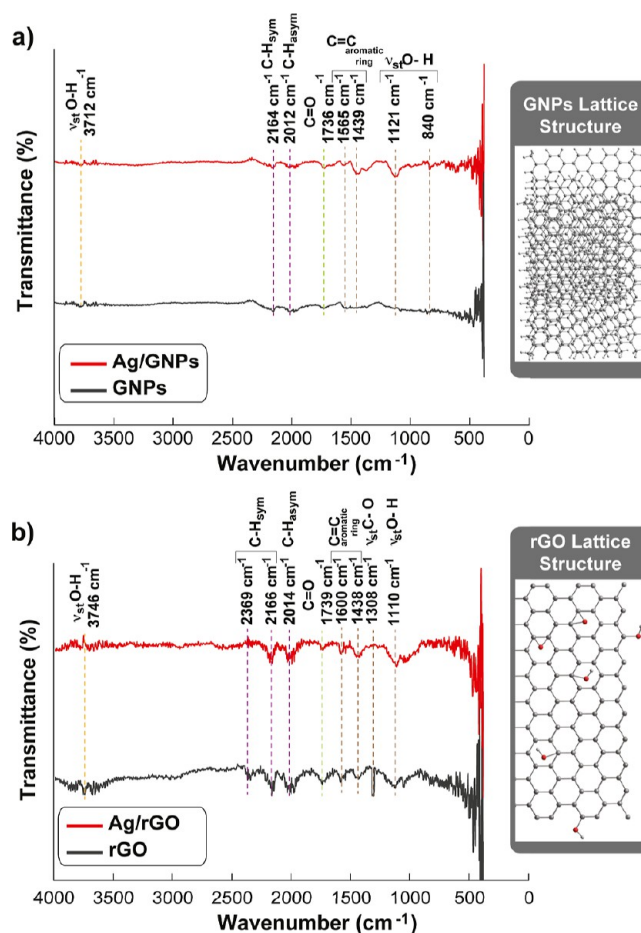

Figure 2. FTIR spectra of nanostructured carbon materials: (a) GNPs and Ag/GNPs and (b) rGO and Ag/rGO.

The FTIR spectrum of pristine rGO, as illustrated in Figure 2b, mirrors the vibrational attributes of GNPs. The inherent C=C signals from aromatic rings and symmetric and asymmetric vibrations of carboxyl O=C−O groups are presented at 1400 and 1600 cm^{-1}.[13,36] In addition, C−H symmetrical and asymmetrical signals of the aromatic ring and lattice edge correspond at 2166 and 2014 cm^{-1}. Nonetheless, discernible amplification at 3746 and 1739 cm^{-1}, corresponding to the C=O and the O−H vibrations, emerges. This intensification can be traced to the presence of inherent chemical species, such as phenol, lactone, and a suite of oxygen-bearing functional groups with C−O and O−H stretching vibrations at 1308 and 1110 cm^{-1}, respectively. These groups are intrinsic to the lattice edges of the rGO structure and have been widely reported in the literature.[37−39] The FTIR spectrum of Ag/rGO (Figure 2b) aligns with the vibrational bands of rGO. Yet a slight increase in intensity is evident, stemming from the integration of the d-orbitals of the anchored Ag-NPs into the oxygenated graphitic lattice.

In concordance with the research demonstrated by Das et al., the antimicrobial efficacy of rGO is primarily attributed to its capability to physically alter the bacterial cell wall through the generation of ROS such as hydrogen peroxide (H$_2$O$_2$), superoxide anions (O$_2$•$^−$), hydroxyl radicals (OH•), or singlet molecular oxygen (^{1}O$_2$), disabling respiratory chain enzymes and inducing the leakage of intracellular materials. In the present study, the persistence of ROS, coupled with the constructive rehybridization maintaining the sp^2 hybridization
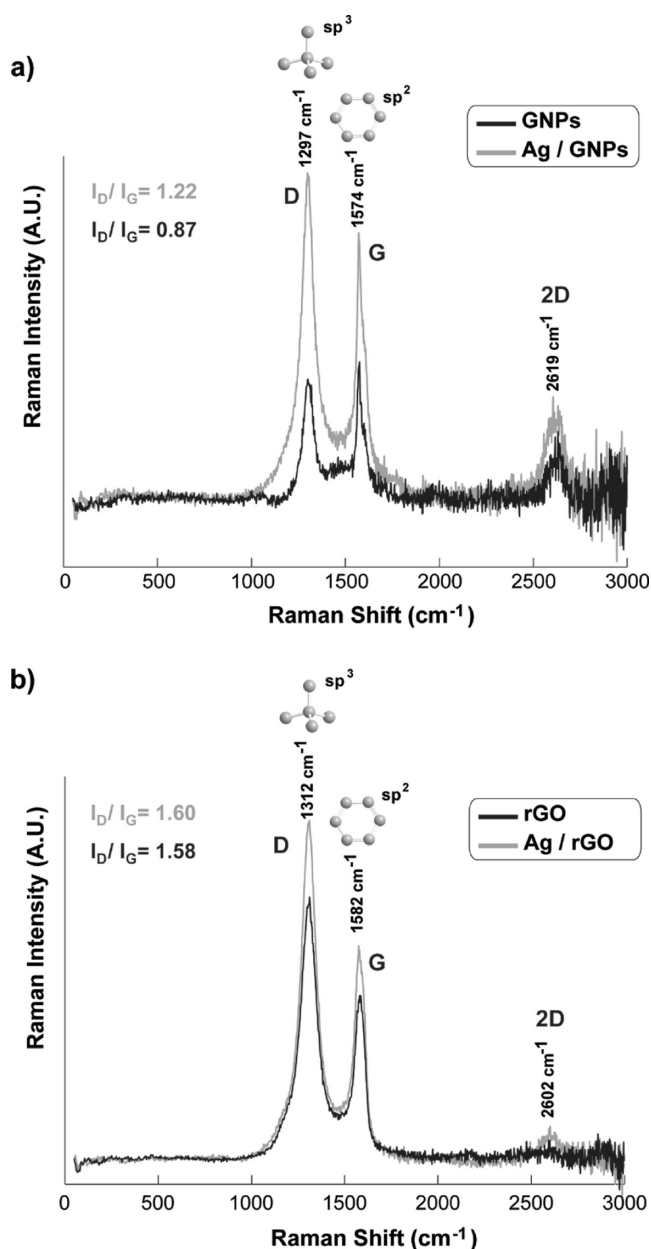
Figure 3. Raman spectra of nanostructured carbon materials: (a) GNPs and Ag/GNPs and (b) rGO and Ag/rGO.
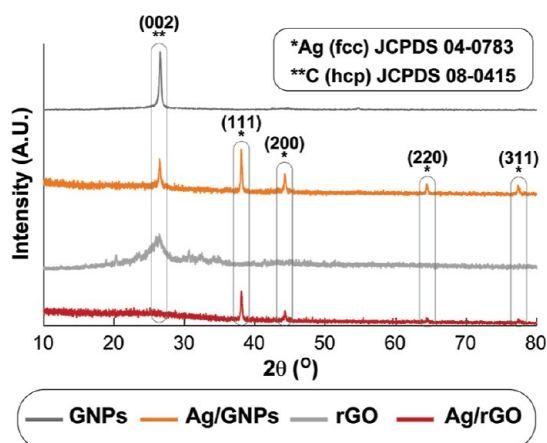
Figure 4. XRD patterns of GNPs, Ag/GNPs, rGO, and Ag/rGO.

Table 1. XRD Structural Parameters of Ag/GNPs

hkl	2θ degrees	fwhm	D crystallite size (nm)
(111)	38.09	0.209	39
(200)	44.28	0.268	30
(220)	64.44	0.327	25
(311)	77.43	0.417	19

Table 2. XRD Structural Parameters of Ag/rGO

hkl	2θ degrees	fwhm	D crystallite size (nm)
(111)	38.09	0.259	31
(200)	44.29	0.300	27
(220)	64.48	0.370	22
(311)	77.45	0.412	20

of Ag/rGO and Ag/GNPs despite the inclusion of Ag-NPs, highlights the ability of rGO and GNPs to interact with lipopolysaccharides and cell membrane proteins through hydrogen bonding, $\pi-\pi$ stacking, and electrostatic interactions similar to those described by Das et al. This interaction results in the physical disruption of the cell membrane and alters the transmembrane potential. The membrane permeabilization leads to the leakage of intracellular substances, including proteins and nucleic acids, causing cellular inactivation, as extensively demonstrated in highly relevant research by Das et al.[12,13]

Transitioning to Figure 3a, the Raman spectra cast light into the crystalline architecture, supported by the sp^2 hybridization of the G-band within the GNPs' honeycomb lattice and the subsequent inclusion of d-orbitals from Ag atoms in Ag/GNPs. The G-band at 1574 cm^{-1} shows no significant change in the sp^2 hybridization in the aromatic lattice or only a slight increment, subtly underscoring the preservation of the electronic graphitic structure of the aromatic ring in the GNPs. The I_D/I_G ratio, calculated by juxtaposing the intensities of the D-band (found at 1297 cm^{-1}) against the G-band, increases from 0.87 in GNPs to 1.22 in Ag/GNPs. This increment corroborates the preservation of the graphitic structure of the honeycomb lattice in the GNPs, without significant distortion or an increment in sp^3 hybridization. In addition, the 2-D band, appearing at 2619 cm^{-1} in both GNPs and Ag/GNPs, reflects the electron−phonon interaction of the 2-D graphitic layer stacked in the pristine GNPs. The increment in the 2-D band signal intensity in Ag/GNPs emerges from electronic overlapping between the π-orbitals of the GNPs and the d-orbitals of the anchored silver atoms. A similar behavior has been reported by Cong et al. when nanostructured carbon materials such as graphene are doped with metallic atoms of the d-block.[40]

In the Raman spectrum presented in Figure 3b, the d-band appearing at 1312 cm^{-1} underscores the presence of sp^3 hybridization, which is indicative of oxygenated functional groups within the rGO architecture. This observation supports the existence of phenol, lactone, and other oxygenated functional groups anchored to the boundaries of rGO, a finding in alignment with the studies by Lesiak et al. on a similar nanostructured carbon lattice.[38] Furthermore, the presence and prevalence of the G-band at 1582 cm^{-1} suggest elucidation of the electronic interaction between the π-orbitals of the sp^2 hybridization of the honeycomb structure and the d-orbitals of the introduced Ag transition metal. This is added to the electronic interaction between oxygenated reactive groups
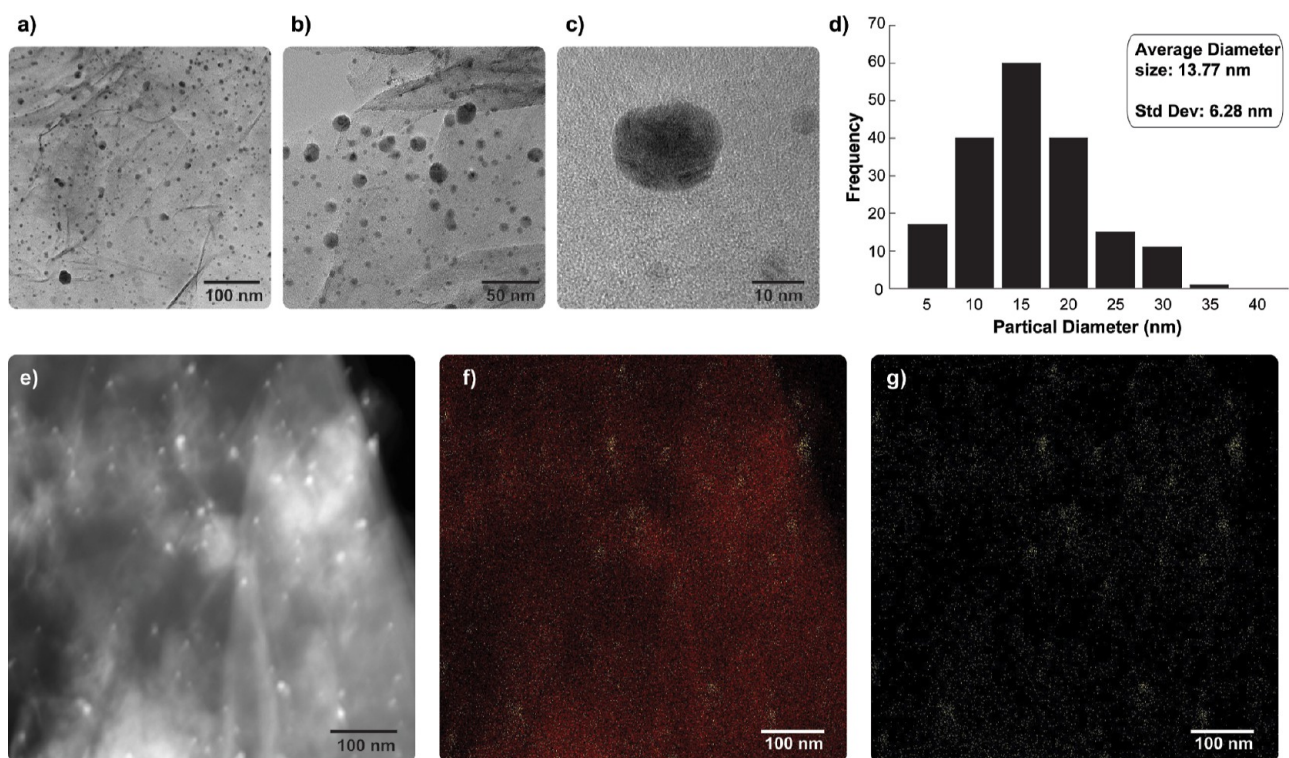
Figure 5. HR-TEM analysis micrographs of Ag/GNPs at different scales: (a) 100, (b) 50, and (c) 10 nm. (d) Histogram that demonstrates the size distributions of the AgNPs. (e) STEM-HAADF image and chemical mapping of Ag/GNPs in EDS, (f) carbon, and (g) silver.
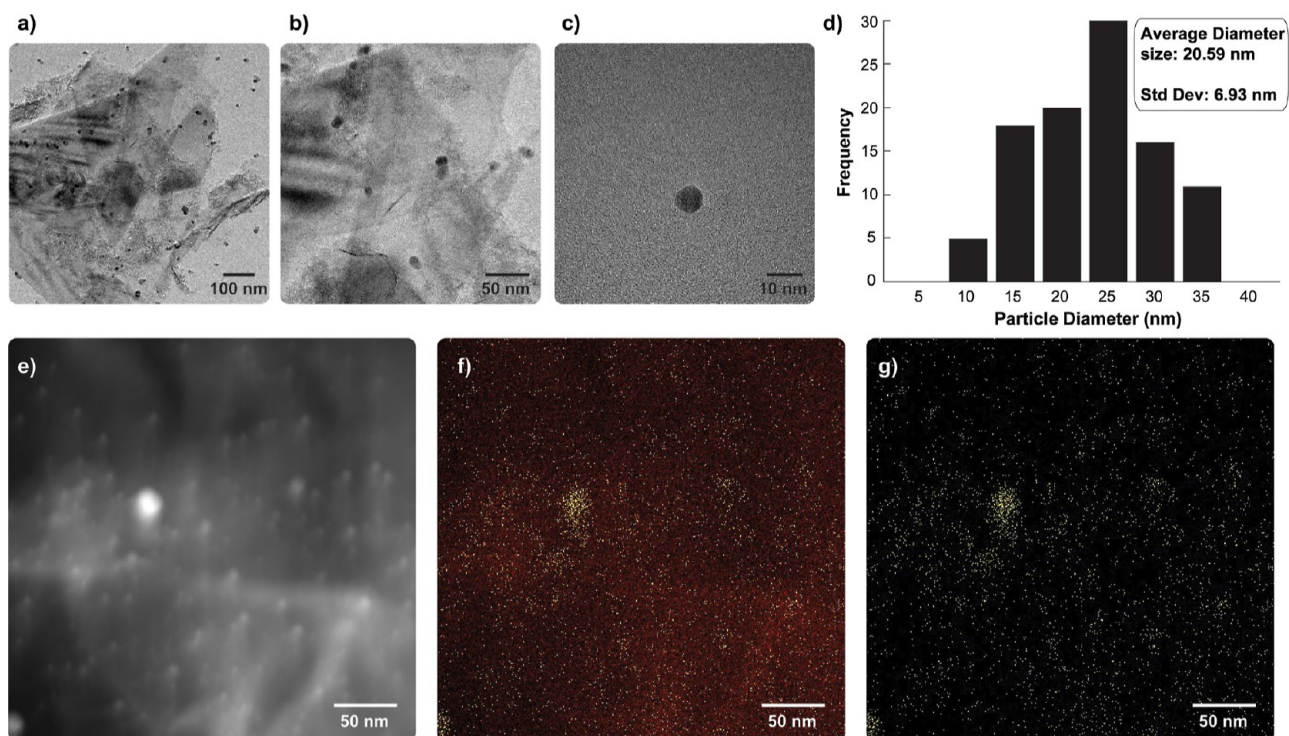
Figure 6. HR-TEM analysis micrographs of Ag/rGO at different scales: (a) 100, (b) 50, and (c) 10 nm. (d) Histogram that demonstrates the size distributions of the AgNPs. (e) STEM-HAADF image and chemical mapping of Ag/rGO in EDS, (f) carbon, and (g) silver.

and AgNPs, which effectively diminishes the disorder-induced band. Nonetheless, the presence of a subtle 2-D band at 2062 cm^{-1} can be ascribed to π-electron dispersion energies, a byproduct of interactions between the stacked graphitic lattices.[41]

In the XRD pattern for Ag/GNPs, presented in Figure 4, distinct characteristic crystal reflections indicative of metallic silver are observed: (111), (200), (220), and (311) at 2θ values of 38.09, 44.28, 64.44, and 77.43°, respectively (JCPDS 04-0783).[42,43] Concurrently, the crystal structure of the
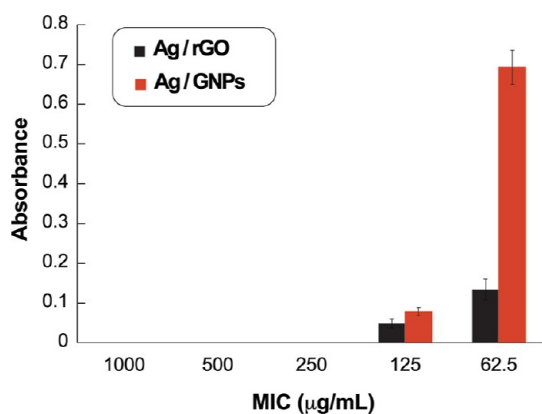
Figure 7. MIC of Ag/rGO and Ag/GNPs.

graphitic carbon lattice from GNPs is evident at $2\theta = 26.44°$, aligning with the (002) crystal reflection of pristine carbon. The XRD pattern for GNPs reveals only the crystal reflection of graphitic carbon at $2\theta = 26.44°$ (Figure 4), in accordance with file JCPDS card no. 08-0415.[44,45] Figure 4 also unveils the hexagonal close-packed (hcp) (002) crystal reflection of pristine rGO at $2\theta = 26.20°$. This broad and slightly curved peak contrasts with the narrow peak observed for GNPs. Such different peak shapes are attributed to imperfections and oxygen-bearing groups in rGO, inducing distortions in its crystal arrangement despite its high degree of graphitization.[46]

Furthermore, the XRD pattern for Ag/rGO (Figure 4) delineates the metallic silver planes represented by the (111), (200), (220), and (311) crystal reflections at their respective 2θ values.[47] The (002) crystal reflection of rGO is represented as a slight signal at $2\theta = 26.01°$. Tables 1 and 2 display the crystal sizes for Ag/GNPs and Ag/rGO. The average crystallite size for Ag/GNPs is approximately 28 nm, whereas Ag/rGO is 25 nm. Notably, the XRD-detected crystallite dimensions across all reflections represent the minimal grain boundary detected by the XRD radiation. Nonetheless, a comprehensive understanding of Ag-NP size, morphology, and distribution

across the carbon lattices is attained via HR-TEM and STEM analyses.

HR-TEM analysis of Ag/GNPs was conducted at different resolutions: 100, 50, and 10 nm (Figure 5a–c, respectively). Figure 5a unveils the GNP lattice, showcasing anchored Ag-NPs within the overlapped carbon layers. A notable observation from Figure 5b is the tendency of Ag-NPs to coalesce, in congruence with the crystallite size of approximately 28 nm calculated from the XRD measurement data (Table 1). The hcp crystal array of GNPs discerned here potentially fosters the clustering of Ag-NPs. Kamyshny et al. have posited that an unusual hcp crystalline structure of Ag-NPs might emerge when their self-assembly is influenced by water evaporation, thereby triggering clustering effects.[48] Delving deeper, Figure 5c shows the distinct morphologies and shapes of Ag-NPs with an average size of 13.77 (Figure 5d). This distinctive formation can be attributed to the polyol method, which allows simultaneous synthesis and anchoring of Ag-NPs onto the GNP surface.[49]

In Figure 5c, we observe Ag-NPs with diameters below 10 nm anchored onto the GNP surface. The high-angle annular dark-field STEM (HAADF-STEM) image and chemical mapping for Ag/GNPs are shown in Figure 5e–g. These images are presented in a color-coded format and correspond to Ag-NPs, which are homogeneously distributed across the substrate (Figure 5e–g). Turning our attention to Ag/rGO (Figure 6), we found a lower degree of coalescence among the Ag-NPs (Figure 6a–c), resulting in nanoparticles averaging 20.59 nm in size (Figure 6d). This result aligns with the crystallite dimensions calculated from the XRD data (Table 2). Figure 6b,c highlights coalesced Ag-NPs, with the darker, larger spots exceeding 10 nm and the lighter gray indicating dispersed Ag-NPs smaller than 5 nm.[25]

Figure 6e–g presents the STEM-HAADF images and chemical mapping of Ag/rGO. This analysis captures the high dispersion of bright spots, indicative of Ag-NPs, across the rGO substrate.[50] The comprehensive physicochemical characterization of Ag/GNPs and Ag/rGO underscores the feasibility

Table 3. Concentration of rGO, GNPs, Ag/rGO, and Ag/GNPs

material/concentration	Ag-NPs/$\mu g\ mL^{-1}$	rGO/$\mu g\ mL^{-1}$	GNPs/$\mu g\ mL^{-1}$
rGO		1000	
		500	
		250	
		125	
		62.5	
GNPs			1000
			500
			250
			125
			62.5
Ag/rGO	200	800	
	100	400	
	50	200	
	25	100	
	12.5	50	
Ag/GNPs	200		800
	100		400
	50		200
	25		100
	12.5		50
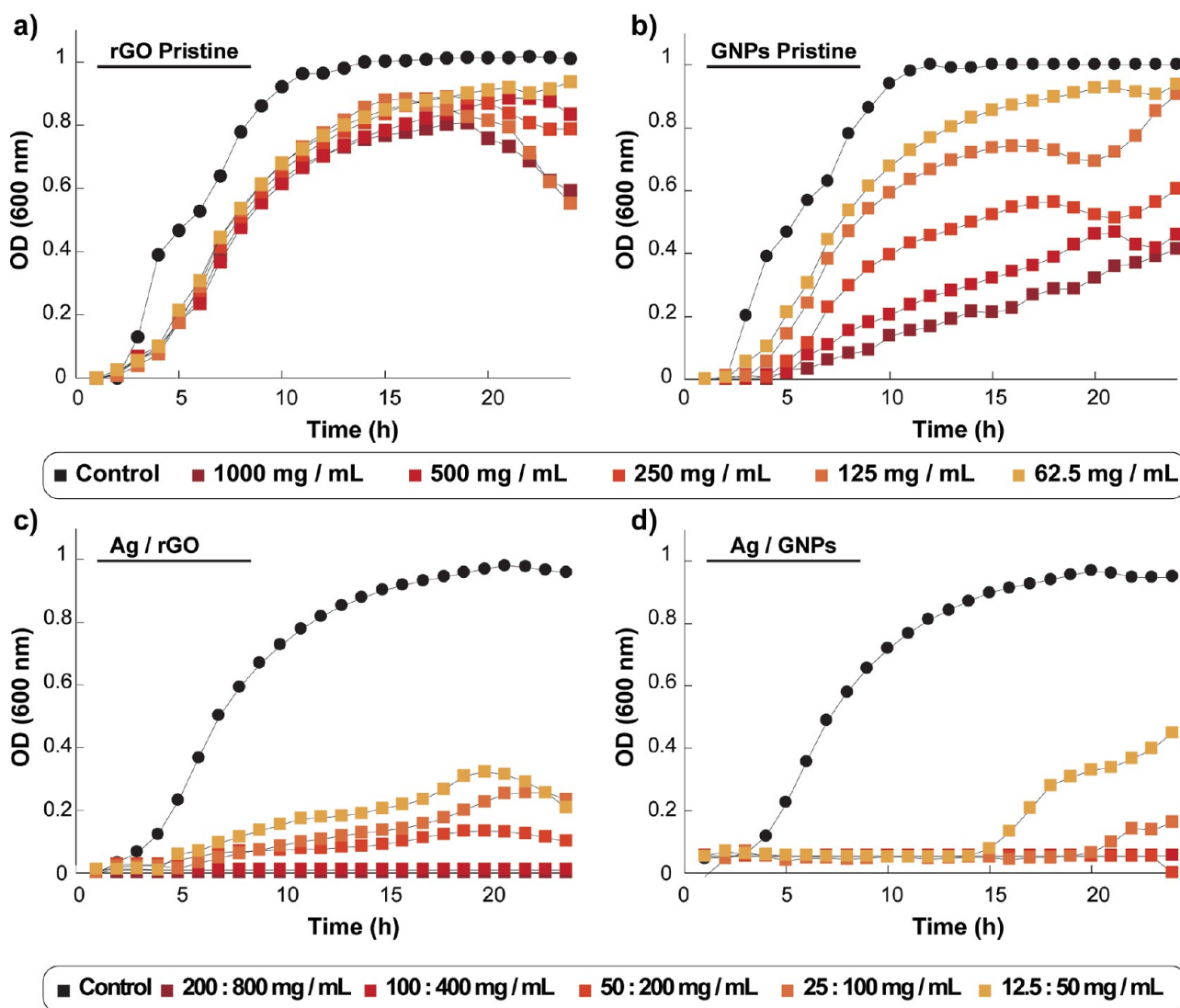
Figure 8. Curves of the kinetic growth of *E. coli* (ATCC-11229) comparing the control with several concentrations of (a) rGO pristine, (b) GNPs pristine, (c) Ag/rGO, and (d) Ag/GNPs.

of the polyol method in achieving well-distributed, nanoscaled Ag-NPs, which enhances the properties of nanostructured carbon supports. Subsequently, these engineered nanomaterials were evaluated as antimicrobial agents, focusing on their potential interactions with the irregular surfaces of microbial cell walls, a phenomenon previously reported by Rago et al.[24] For the purposes of this investigation, we used *E. coli* (*E. coli* ATCC-11229) to evaluate the bactericidal activity of rGO, GNPs, Ag/rGO, and Ag/GNPs.
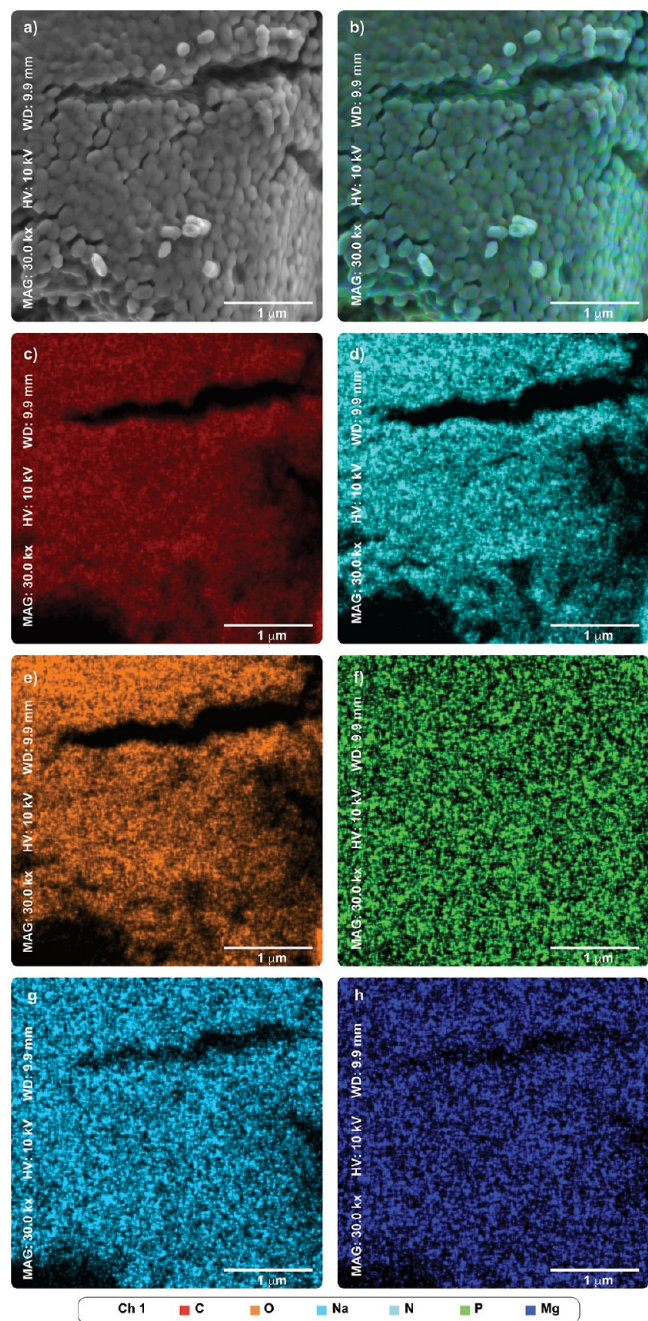
3.2. Antimicrobial Evaluation. In the present study, MIC results revealed that the carbon nanostructures decorated with Ag-NP exhibit potent activities against all tested bacteria. The antimicrobial activity of the carbon nanostructures decorated with Ag-NP was determined by exposing the *E. coli* ATCC 11229 bacteria with different concentrations of Ag/rGO and Ag/GNPs, which can be seen in Figure 7, where the values of the MICs of Ag/rGO and Ag/GNPs were 50 μg/mL with both nanostructures; however, we can observe that there is a significant difference between them since Ag/rGO showed to have a greater antimicrobial effect.

Table 3 records the concentrations of pristine and hybrid graphitic materials: rGO, GNPs, Ag/rGO, and Ag/GNPs, all diluted in the LB medium to which *E. coli* was exposed.

Figure 8 shows the *E. coli* growth kinetic curves: the control and subsequent exposure to different concentrations of rGO and GNPs. The control growth exhibits the typical lag, exponential, and stationary phases. The introduction of rGO induces a slope change of around 16 to 21 h across all concentrations of the carbonaceous material, indicating a bacterial inhibitory effect. On the other hand, GNPs cause a significant decrease in OD_{600nm} within the 125 and 1000 μg mL^{-1} range. Additionally, an atypical stationary phase behavior across all concentrations suggests the potential of GNPs to trap and wrap the bacterial cell wall. This could inhibit growth due to cellular ruptures and constriction induced by the hard and sharp edges of GNPs.[24]

Further analyses in Figure 8c and d depict the *E. coli* growth kinetics in the presence of Ag/rGO and Ag/GNPs, aiming to evaluate their antimicrobial effects. The control growth demonstrated a slight decrease in the OD_{600nm} during the exponential phase due to pristine rGO and GNPs. Notably, a pronounced decline in *E. coli* growth, particularly with Ag/

Figure 10. SEM images of (a) pristine *E. coli* (ATCC-11229) and (b) *E. coli* before the coating with Ag/rGO.

Figure 11. SEM images of *E. coli* recovered: (a) Ag/rGO 12.5 μg mL^{-1}, (b) Ag/rGO 200 μg mL^{-1}, (c) Ag/GNPs 12.5 μg mL^{-1}, and (d) Ag/GNPs 200 μg mL^{-1}.
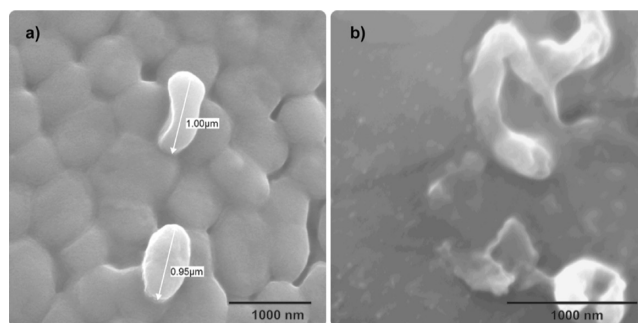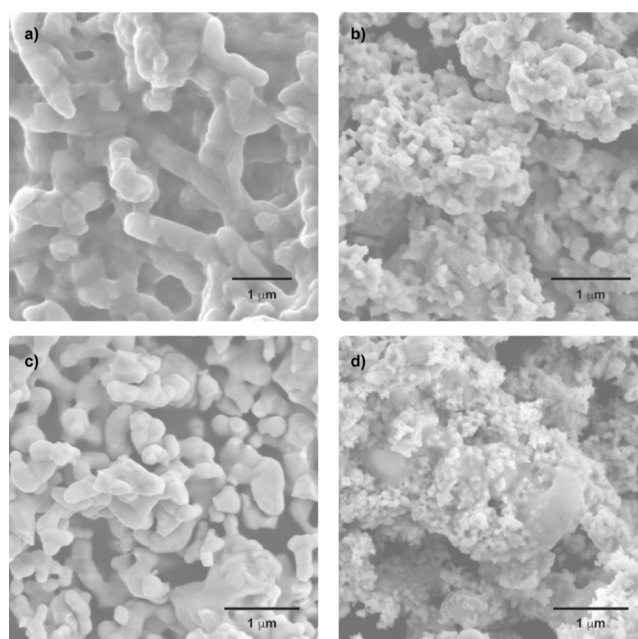

Figure 9. SEM–EDS micrograph of *E. coli* (ATCC-11229); (b) chemical mapping (color-coded): (c) carbon, C; (d) oxygen, O; (e) sodium, Na; (f) nitrogen, N; (g) phosphorus, P; and (h) magnesium, Mg.

GNPs, suggested a synergistic effect. This effect combined the bactericidal action of Ag-NPs with the entrapping-wrapping capabilities of GNPs, culminating in *E. coli* cell eradication. Effective concentrations range from (Ag: carbon nano-structured material, rGO, or GNPs) 50:200 to Ag/rGO and 25:100 μg mL^{-1} to Ag/GNPs. These results agree with the determined MIC, yielding values of 25 and 12.5 mg mL^{-1} for Ag/rGO and Ag/GNPs, respectively.

The SEM–EDS micrograph in Figure 9a shows the *E. coli* cellular wall structure. Evidently, bacterial colonies grown in the LB medium adopt a layered surface configuration consisting of cylindrical and spherical bacilli. Chemical

mapping (Figure 9b−h) identified the presence of C, O, Na, P, and Mg within the bacterial structure. The bacterial morphology displayed in Figure 8a,b is captured in a cross-sectional view, showing both cylindrical and spherical shapes.

On the other hand, Figure 10a offers a unique perspective, showcasing two bacteria not in a layered configuration, attributed to nonstacked isolated *E. coli* bacilli. Both manifest a cylindrical shape, each approximating 1 μm in length. Moreover, Figure 10b shows the cell surface of the bacteria severely disrupted before being coated with the MIC of Ag/ rGO (50 μg/mL), this behavior is similar to that widely reported by Parandhaman and Das, where it was described that the interaction of rGOAg with bacterial cells often produces the formation of ROS, such as hydroxyl radicals (OH$^{\bullet}$), superoxide ions (O$_2^{\bullet-}$), hydrogen peroxide (H$_2$O$_2$), and hydroperoxyl radicals (HO$_2^{\bullet-}$), which induces oxidative stress in the cells and a strong damage to proteins and nucleic acids, leading to cell death.[11]

The SEM micrographs presented in Figure 11a,b depict the morphology of *E. coli* biofilms in the presence of both the lowest and highest concentrations of Ag/rGO, specifically 12.5:50 μg mL^{-1} and 200:800 μg mL^{-1}, respectively. At the

lowest concentration, *E. coli* forms a robust matrix, indicative of healthy bacterial growth. In contrast, the highest concentration reveals a fragmented *E. coli* bacterial matrix interspersed with small, irregularly shaped bacteria. Some Ag/rGO particles can be observed as well. These observations underscore the combined bactericidal action, trapping-wrapping effect, and resulting bactericidal activity due to the strong interaction between Ag-NPs and rGO.

Figure 11c,d shows SEM micrographs of *E. coli* biofilms subjected to the lowest and highest concentrations of Ag/GNPs, paralleling the concentrations (12.5:50 and 200:800 μg mL^{-1}, respectively). Interestingly, at the lowest concentration, there is limited growth of the *E. coli* biofilm, with only some Ag/GNPs interspersed. The visual evidence testifies to the potent bactericidal interaction between Ag-NPs and GNPs, resulting in shrinkage and severe damage to *E. coli*. Upon exposure to the highest concentration, the bacterial integrity is completely compromised, as evidenced by severe damage to the *E. coli* cellular wall, inhibiting extracellular matrix development. Though smaller, irregular bacterial entities are identifiable, they do not resonate with the characteristic morphology of *E. coli*. Notably, scattered Ag/GNPs are visible, devoid of any bacterial presence. Such observations suggest that among the materials assessed, Ag/GNPs exhibit the most pronounced antimicrobial potency.

4. CONCLUSIONS

This study elucidates the synergistic effect of metal−organic interactions in Ag/rGO and Ag/GNP materials, affirming their potential as antimicrobial agents. Explicitly, their mechanical damage against *E. coli* (ATCC-11229) was evidenced through SEM−EDS micrographs under low vacuum, revealing the cellular disruptions and shrinking instigated by the sharp edges of the carbon-based systems. Delving deeper, HR-TEM and STEM-HAADF imaging of the Ag/rGO and Ag/GNP materials accentuates the remarkable dispersion and homogeneity of the spherically shaped Ag-NPs that decorate the carbon lattices. This homogeneous arrangement increases the concentration and contact area of the Ag-NPs with the bacterial cell wall, increasing their bactericidal potential.

Notably, the inherent toxicity of the uniformly dispersed spherical Ag-NPs, coupled with their association with the carbon lattices, significantly bolsters their bactericidal effect. This is evident from the compelling MIC values exhibited at 50.0 μg mL^{-1} for Ag/rGO and Ag/GNPs, respectively. Such findings not only accentuate their relevance but also pave the way for their prospective incorporation in advanced antimicrobial systems and sophisticated biosensors. The hybrid metal−organic synergy of these systems could be a cornerstone for the next generation of devices, merging the benefits of both domains.

Looking forward, the scalability and adaptability of this synthesis approach can be further optimized to cater to various microbial strains, potentially expanding the spectrum of its antimicrobial activity. Additionally, understanding the detailed kinetics of bacterial cell interactions will offer insights for controlled release applications, optimizing the longevity of antimicrobial effects. While the primary focus of this study has been to establish the antimicrobial potential of metal−organic nanostructured carbon materials, their distinctive physicochemical properties may hold promise for future applications in areas such as environmental sensing and catalysis. The current exploration of such hybrid systems underlines the value of interdisciplinary research in developing solutions to complex scientific challenges.

■ AUTHOR INFORMATION

Corresponding Author

  José Rubén Morones-Ramírez − *Facultad de Ciencias Químicas (FCQ), Universidad Autónoma de Nuevo León (UANL), San Nicolás de los Garza, Nuevo León C.P. 66455, Mexico; Centro de Investigación en Biotecnología y Nanotecnología CIByN-FCQ-UANL, Parque Industrial Innovación Tecnológica, Apodaca, Nuevo León C.P. 66628, Mexico;* orcid.org/0000-0001-7009-686X; Email: jose.moronesrmr@uanl.edu.mx

Authors

  Adriana Angelina Siller-Ceniceros − *Facultad de Ciencias Químicas (FCQ), Universidad Autónoma de Nuevo León (UANL), San Nicolás de los Garza, Nuevo León C.P. 66455, Mexico; Centro de Investigación en Biotecnología y Nanotecnología CIByN-FCQ-UANL, Parque Industrial Innovación Tecnológica, Apodaca, Nuevo León C.P. 66628, Mexico*

  Dulce Carolina Almonte-Flores − *Facultad de Ciencias Químicas (FCQ), Universidad Autónoma de Nuevo León (UANL), San Nicolás de los Garza, Nuevo León C.P. 66455, Mexico; Centro de Investigación en Biotecnología y Nanotecnología CIByN-FCQ-UANL, Parque Industrial Innovación Tecnológica, Apodaca, Nuevo León C.P. 66628, Mexico*

  M. Esther Sánchez-Castro − *Nanociencias y Nanotecnología, Cinvestav Unidad Saltillo, Ramos Arizpe, Coahuila C.P. 25900, Mexico; Sustentabilidad de los Recursos Naturales y Energía, Cinvestav Unidad Saltillo, Ramos Arizpe 25900, Mexico*

  Eduardo Martínez-Guerra − *Centro de Investigación en Materiales Avanzados (CIMAV Unidad Monterrey), Apodaca, Nuevo León C.P. 66600, Mexico;* orcid.org/0000-0002-2308-1259

  Javier Rodríguez-Varela − *Nanociencias y Nanotecnología, Cinvestav Unidad Saltillo, Ramos Arizpe, Coahuila C.P. 25900, Mexico; Sustentabilidad de los Recursos Naturales y Energía, Cinvestav Unidad Saltillo, Ramos Arizpe 25900, Mexico;* orcid.org/0000-0002-1042-7628

  Nora Aleyda García Gómez − *Facultad de Ciencias Químicas (FCQ), Universidad Autónoma de Nuevo León (UANL), San Nicolás de los Garza, Nuevo León C.P. 66455, Mexico; Centro de Investigación en Biotecnología y Nanotecnología CIByN-FCQ-UANL, Parque Industrial Innovación Tecnológica, Apodaca, Nuevo León C.P. 66628, Mexico*

Complete contact information is available at:
https://pubs.acs.org/10.1021/acsomega.3c08634

Notes

The authors declare no competing financial interest.

■ REFERENCES

(1) Wang, T.; Wusigale; Kuttappan, D.; Amalaradjou, M. A.; Luo, Y.; Luo, Y. Polydopamine-coated chitosan hydrogel beads for synthesis and immobilization of silver nanoparticles to simultaneously enhance antimicrobial activity and adsorption kinetics. *Adv. Compos. Hybrid Mater.* **2021**, *4*, 696−706.

(2) Dat, N. M.; Thinh, D. B.; Huong, L. M.; Tinh, N. T.; Linh, N. T. T.; Hai, N. D.; Viet, N. D.; Dat, N. T.; Phong, M. T.; Hieu, N. H. Facile synthesis and antibacterial activity of silver nanoparticles-modified graphene oxide hybrid material: the assessment, utilization, and anti-virus potentiality. *Mater. Today Chem.* **2022**, *23* (2022), 100738.

(3) Goda, E. S.; Abu Elella, M. H.; Sohail, M.; Singu, B. S.; Pandit, B.; El Shafey, A. M.; Aboraia, A. M.; Gamal, H.; Hong, S. E.; Yoon, K. R. N-methylene phosphonic acid chitosan/graphene sheets decorated with silver nanoparticles as green antimicrobial agents. *Int. J. Biol. Macromol.* **2021**, *182*, 680−688.

(4) Pal, N.; Banerjee, S.; Roy, P.; Pal, K. Cellulose nanocrystals-silver nanoparticles-reduced graphene oxide based hybrid PVA nano-composites and its antimicrobial properties. *Int. J. Biol. Macromol.* **2021**, *191*, 445−456.

(5) Bamal, D.; Singh, A.; Chaudhary, G.; Kumar, M.; Singh, M.; Rani, N.; Mundlia, P.; Sehrawat, A. R. Silver Nanoparticles Biosynthesis, Characterization, Antimicrobial Activities, Applications, Cytotoxicity and Safety Issues: An Updated Review. *Nanomaterials* **2021**, *11*, 2086.

(6) Singh, P.; Pandit, S.; Jers, C.; Joshi, A. S.; Garnæs, J.; Mijakovic, I. Silver nanoparticles produced from Cedecea sp. exhibit antibiofilm activity and remarkable stability. *Sci. Rep.* **2021**, *11*, 12619.

(7) Mikhailova, E. O. Silver Nanoparticles: Mechanism of Action and Probable Bio-Application. *J. Funct. Biomater.* **2020**, *11*, 84.

(8) McNeilly, O.; Mann, R.; Hamidian, M.; Gunawan, C. Emerging Concern for Silver Nanoparticle Resistance in Acinetobacter baumannii and Other Bacteria. *Front. Microbiol.* **2021**, *12*, 652863.

(9) Anees Ahmad, S.; Sachi Das, S.; Khatoon, A.; Tahir Ansari, M.; Afzal, M.; Saquib Hasnain, M.; Kumar Nayak, A. Bactericidal activity of silver nanoparticles: A mechanistic review. *Mater. Sci. Energy Technol.* **2020**, *3*, 756−769.

(10) Abbaszadegan, A.; Ghahramani, Y.; Gholami, A.; Hemmateenejad, B.; Dorostkar, S.; Nabavizadeh, M.; Sharghi, H. The Effect of Charge at the Surface of Silver Nanoparticles on Antimicrobial Activity against Gram-Positive and Gram-Negative Bacteria: A Preliminary Study. *J. Nanomater.* **2015**, *2015*, 720654.

(11) Parandhaman, T.; Das, S. K. Facile synthesis, biofilm disruption properties and biocompatibility study of a poly-cationic peptide functionalized graphene−silver nanocomposite. *Biomater. Sci.* **2018**, *6*, 3356−3372.

(12) Parandhaman, T.; Choudhary, P.; Ramalingam, B.; Schmidt, M.; Janardhanam, S.; Das, S. K. Antibacterial and Antibiofouling Activities of Antimicrobial Peptide-Functionalized Graphene-Silver Nanocomposites for the Inhibition and Disruption of Staphylococcus aureus Biofilms. *ACS Biomater. Sci. Eng.* **2021**, *7*, 5899−5917.

(13) Choudhary, P.; Parandhaman, T.; Ramalingam, B.; Duraipandy, N.; Kiran, M. S.; Das, S. K. Fabrication of Nontoxic Reduced Graphene Oxide Protein Nanoframework as Sustained Antimicrobial Coating for Biomedical Application. *ACS Appl. Mater. Interfaces* **2017**, *9*, 38255−38269.

(14) Fathalipour, S.; Pourbeyram, S.; Sharafian, A.; Tanomand, A.; Azam, P. Biomolecule-assisted synthesis of Ag/reduced graphene oxide nanocomposite with excellent electrocatalytic and antibacterial performance. *Mater. Sci. Eng., C* **2017**, *75*, 742−751.

(15) Xia, M. Y.; Xie, Y.; Yu, C. H.; Chen, G. Y.; Li, Y. H.; Zhang, T.; Peng, Q. Graphene-based nanomaterials: the promising active agents for antibiotics-independent antibacterial applications. *J. Controlled Release* **2019**, *307*, 16−31.

(16) Malik, S. B.; Saggu, J. I.; Gul, A.; Abbasi, B. A.; Iqbal, J.; Waris, S.; Jardan, Y. A. B.; Chalgham, W. Synthesis and Characterization of Silver and Graphene Nanocomposites and Their Antimicrobial and Photocatalytic Potentials. *Molecules* **2022**, *27*, 5184.

(17) Prasad, K.; Lekshmi, G. S.; Ostrikov, K.; Lussini, V.; Blinco, J.; Mohandas, M.; Vasilev, K.; Bottle, S.; Bazaka, K.; Ostrikov, K. Synergic bactericidal effects of reduced graphene oxide and silver nanoparticles against Gram-positive and Gram-negative bacteria. *Sci. Rep.* **2017**, *7*, 1591.

(18) Morones, J. R.; Elechiguerra, J. L.; Camacho, A.; Holt, K.; Kouri, J. B.; Ramírez, J. T.; Yacaman, M. J. The bactericidal effect of silver nanoparticles. *Nanotechnology* **2005**, *16*, 2346−2353.

(19) Chen, J. P.; Lim, L. L. Key factors in chemical reduction by hydrazine for recovery of precious metals. *Chemosphere* **2002**, *49*, 363−370.

(20) Yang, L.; Yan, W.; Wang, H.; Zhuang, H.; Zhang, J. Shell thickness-dependent antibacterial activity and biocompatibility of gold@silver core-shell nanoparticles. *RSC Adv.* **2017**, *7*, 11355−11361.

(21) Shanmuganathan, R.; Sathishkumar, G.; Brindhadevi, K.; Pugazhendhi, A. Fabrication of naringenin functionalized-Ag/RGO nanocomposites for potential bactericidal effects. *J. Mater. Res. Technol.* **2020**, *9*, 7013−7019.

(22) Chen, L.; Li, Z.; Chen, M. Facile production of silver-reduced graphene oxide nanocomposite with highly effective antibacterial performance. *J. Environ. Chem. Eng.* **2019**, *7*, 103160.

(23) Zhao, T.; Sun, R.; Yu, S.; Zhang, Z.; Zhou, L.; Huang, H.; Du, R. Size-controlled preparation of silver nanoparticles by a modified polyol method. *Colloids Surf., A* **2010**, *366*, 197−202.

(24) Rago, I.; Bregnocchi, A.; Zanni, E.; D'Aloia, A. G.; De Angelis, F.; Bossu, M.; De Bellis, G.; Polimeni, A.; Uccelletti, D.; Sarto, M. S. Antimicrobial activity of graphene nanoplatelets against Streptococcus mutans. *IEEE-NANO 2015—15th International Conference on Nano-technology*, 2015; Vol. *2015*, pp 9−12.

(25) Geetha Bai, R.; Muthoosamy, K.; Shipton, F. N.; Pandikumar, A.; Rameshkumar, P.; Huang, N. M.; Manickam, S. The biogenic synthesis of a reduced graphene oxide-silver (RGO-Ag) nano-composite and its dual applications as an antibacterial agent and cancer biomarker sensor. *RSC Adv.* **2016**, *6*, 36576−36587.

(26) Siller-Ceniceros, A. A.; Sánchez-Castro, E.; Morales-Acosta, D.; Torres-Lubián, J. R.; Martínez-Guerra, E.; Rodríguez-Varela, J. Functionalizing Reduced Graphene Oxide with Ru-Organometallic Compounds as an Effective Strategy to Produce High-Performance Pt Nanocatalysts for the Methanol Oxidation Reaction. *ChemElectro-Chem* **2019**, *6*, 4902−4916.

(27) Mehta, B. K.; Chhajlani, M.; Shrivastava, B. D. Green synthesis of silver nanoparticles and their characterization by XRD. *J. Phys.: Conf. Ser.* **2017**, *836*, 012050.

(28) Sarabia-Castillo, C. R.; Pérez-Moreno, A. Y.; Fernández-Luqueño, F. Metal Oxide Nanoparticles (Tio 2, Zno, and Fe 2 O 3) Change the Functional Groups, but not the Plant Tissue Content of Common Bean Plants Grown in a Greenhouse. *Pol. J. Environ. Stud.* **2023**, *32*, 1343−1352.

(29) Garza-Cervantes, J. A.; Chávez-Reyes, A.; Castillo, E. C.; García-Rivas, G.; Antonio Ortega-Rivera, O.; Salinas, E.; Ortiz-Martínez, M.; Gómez-Flores, S. L.; Peña-Martínez, J. A.; Pepi-Molina, A.; Treviño-González, M. T.; Zarate, X.; Elena Cantú-Cárdenas, M.; Enrique Escarcega-Gonzalez, C.; Morones-Ramírez, J. R. Synergistic Antimicrobial Effects of Silver/Transition-metal Combinatorial Treat-ments. *Sci. Rep.* **2017**, *7*, 903.

(30) Padilla-Cruz, A. L.; Garza-Cervantes, J. A.; Vasto-Anzaldo, X. G.; García-Rivas, G.; León-Buitimea, A.; Morones-Ramírez, J. R. Synthesis and design of Ag−Fe bimetallic nanoparticles as antimicrobial synergistic combination therapies against clinically relevant pathogens. *Sci. Rep.* **2021**, *11*, 5351.

(31) Tran, V. Q.; Doan, H. T.; Nguyen, N. T.; Do, C. V. Preparation of graphene nanoplatelets by thermal shock combined with ball milling methods for fabricating flame-retardant polymers. *J. Chem.* **2019**, *2019*, 5284160.

(32) Ding, J.-H.; Zhao, H.-R.; Yu, H.-B. A water-based green approach to large-scale production of aqueous compatible graphene nanoplatelets. *Sci. Rep.* **2018**, *8*, 5567.

(33) Meng, Q.; Jin, J.; Wang, R.; Kuan, H.-C.; Ma, J.; Kawashima, N.; Michelmore, A.; Zhu, S.; Wang, C. H. Processable 3-nm thick graphene platelets of high electrical conductivity and their epoxy composites. *Nanotechnology* **2014**, *25*, 125707.

(34) Ramírez-Soria, E. H.; León-Silva, U.; Lara-Ceniceros, T. E.; Advíncula, R. C.; Bonilla-Cruz, J. Reduced Graphene Oxide Nanoplatelets Functionalized with Nonpolar Aliphatic Groups for High-Performance Coatings against Corrosion. *ACS Appl. Nano Mater.* **2022**, *5*, 16760−16773.

(35) Ng, S. W.; Noor, N.; Zheng, Z. Graphene-based two-dimensional Janus materials. *NPG Asia Mater.* **2018**, *10*, 217−237.

(36) Tran, V. Q.; Doan, H. T.; Nguyen, N. T.; Do, C. V. Preparation of Graphene Nanoplatelets by Thermal Shock Combined with Ball Milling Methods for Fabricating Flame-Retardant Polymers. *J. Chem.* **2019**, *2019*, 1−6.

(37) Arrigo, R.; Hävecker, M.; Wrabetz, S.; Blume, R.; Lerch, M.; McGregor, J.; Parrott, E. P. J.; Zeitler, J. A.; Gladden, L. F.; Knop-Gericke, A.; Schlögl, R.; Su, D. S. Tuning the acid/base properties of nanocarbons by functionalization via amination. *J. Am. Chem. Soc.* **2010**, *132*, 9616−9630.

(38) Lesiak, B.; Trykowski, G.; Tóth, J.; Biniak, S.; Kövér, L.; Rangam, N.; Stobinski, L.; Malolepszy, A. Chemical and structural properties of reduced graphene oxide—dependence on the reducing agent. *J. Mater. Sci.* **2021**, *56*, 3738−3754.

(39) Minitha, C. R.; Anithaa, V. S.; Subramaniam, V.; Rajendra Kumar, R. T. Impact of Oxygen Functional Groups on Reduced Graphene Oxide-Based Sensors for Ammonia and Toluene Detection at Room Temperature. *ACS Omega* **2018**, *3*, 4105−4112.

(40) Cong, X.; Liu, X.-L.; Lin, M.-L.; Tan, P.-H. Application of Raman spectroscopy to probe fundamental properties of two-dimensional materials. *npj 2D Mater. Appl.* **2020**, *4*, 13.

(41) Kaniyoor, A.; Ramaprabhu, S. A Raman spectroscopic investigation of graphite oxide derived graphene. *AIP Adv.* **2012**, *2*, 032183.

(42) Chirumamilla, P.; Dharavath, S. B.; Taduri, S. Eco-friendly Green Synthesis of Silver Nanoparticles from Leaf Extract of Solanum khasianum: Optical Properties and Biological Applications. *Appl. Biochem. Biotechnol.* **2023**, *195*, 353−368.

(43) Kanniah, P.; Radhamani, J.; Chelliah, P.; Muthusamy, N.; Joshua Jebasingh Sathiya Balasingh, E.; Reeta Thangapandi, J.; Balakrishnan, S.; Shanmugam, R. Green Synthesis of Multifaceted Silver Nanoparticles Using the Flower Extract of Aerva lanata and Evaluation of Its Biological and Environmental Applications. *ChemistrySelect* **2020**, *5*, 2322−2331.

(44) Safari, M.; de Sousa, R. A.; Salamat-Talab, M.; Joudaki, J.; Ghanbari, D.; Bakhtiari, A. Mechanical Properties of Green Synthesized Graphene Nano-Composite Samples. *Appl. Sci.* **2021**, *11*, 4846.

(45) Kamar, E. M.; Sheha, E. Green synthesis of Co 3 O 4 /graphene nanocomposite as cathode for magnesium batteries. *Mater. Sci.* **2017**, *35*, 528−533.

(46) Jiao, X.; Qiu, Y.; Zhang, L.; Zhang, X. Comparison of the characteristic properties of reduced graphene oxides synthesized from natural graphites with different graphitization degrees. *RSC Adv.* **2017**, *7*, 52337−52344.

(47) Ahamed, M.; Akhtar, M. J.; Khan, M. A. M.; Alhadlaq, H. A. A Novel Green Preparation of Ag/RGO Nanocomposites with Highly Effective Anticancer Performance. *Polymers* **2021**, *13*, 3350.

(48) Grouchko, M.; Popov, I.; Uvarov, V.; Magdassi, S.; Kamyshny, A. Coalescence of silver nanoparticles at room temperature: Unusual crystal structure transformation and dendrite formation induced by self-assembly. *Langmuir* **2009**, *25*, 2501−2503.

(49) Khodashenas, B.; Ghorbani, H. R. Synthesis of silver nanoparticles with different shapes. *Arabian J. Chem.* **2019**, *12*, 1823−1838.

(50) Krishnaraj, C.; Kaliannagounder, V. K.; Rajan, R.; Ramesh, T.; Kim, C. S.; Park, C. H.; Liu, B.; Il Yun, S. Silver nanoparticles decorated reduced graphene oxide: Eco-friendly synthesis, characterization, biological activities and embryo toxicity studies. *Environ. Res.* **2022**, *210*, 112864.